Characterization of springtime leads in the Beaufort/Chukchi Seas from airborne and satellite observations during FIRE/SHEBA

M. A. Tschudi,[1] J. A. Curry,[2] and J. A. Maslanik

Department of Aerospace Engineering Sciences, University of Colorado, Boulder, Colorado, USA

[1] Airborne remote sensing observations in the vicinity of the Surface Heat Budget of the Arctic Ocean (SHEBA) camp in the Beaufort and Chukchi Seas during May 1998 are used to characterize leads. This characterization was accomplished using observations from a passive microwave radiometer, video camera, and infrared pyrometer. An automated methodology is presented to determine lead fraction, width, and orientation. Refrozen lead fraction decreased in the latter half of May, due in part to local convergence in the ice pack. Airborne passive microwave and video observations are combined to produce a lead width distribution for the SHEBA region. Narrow leads are most prevalent, with lead fraction decreasing exponentially with increasing lead width. Lead orientation showed a preference in a northwesterly direction, which is consistent with prevailing wind patterns and ocean circulation. The lead width distribution and lead orientation observed by the airborne sensors are similar to the characteristics derived from an advanced very high resolution radiometer (AVHRR) albedo image encompassing the Beaufort/Chukchi Seas during the same time period. The AVHRR albedos in the SHEBA vicinity are also comparable to the larger region. These similarities suggest that the area of study used by SHEBA investigators was representative of the Western Arctic during this time period for these surface characteristics.   *INDEX TERMS:* 1863 Hydrology: Snow and ice (1827); 3349 Meteorology and Atmospheric Dynamics: Polar meteorology; 4275 Oceanography: General: Remote sensing and electromagnetic processes (0689); 4540 Oceanography: Physical: Ice mechanics and air/sea/ice exchange processes; 9315 Information Related to Geographic Region: Arctic region

Citation: Tschudi, M. A., J. A. Curry, and J. A. Maslanik, Characterization of springtime leads in the Beaufort/Chukchi Seas from airborne and satellite observations during FIRE/SHEBA, *J. Geophys. Res.*, *107*(C10), 8034, doi:10.1029/2000JC000541, 2002.

1. Introduction

[2] Leads are openings in the pack ice that can be produced by thermal stresses, wave action, or local divergence in the floe drift. Typically, arctic leads form long, narrow channels that are tens to hundreds of meters wide and kilometers long. Leads are more prevalent in areas of thin ice, including the marginal ice zones, than in the central Arctic ice pack [*Wadhams et al.*, 1985]. Leads are responsible for about 50% of the sensible heat transfer from the Arctic Ocean to the atmosphere during winter [*Maykut*, 1982], although they cover only a few percent of the surface area. Ice growth rates, turbulent heat exchange into the atmosphere and salt rejection into the ocean can be two orders of magnitude larger over a refreezing lead than over pack ice [*Maykut*, 1982].

[3] The impact of leads on the surface energy budget, upper ocean, ice mass balance and ice dynamics in the Arctic necessitates a realistic representation of the areal coverage of leads by ice models. Width and orientation may also be critical parameters for evaluating the turbulent heat flux from leads. Lead orientation also provides information on the effect of stress on the ice pack and may be used to infer the direction of the forces acting on a particular floe.

[4] During the late spring and summer, leads substantially modify the interactions of shortwave radiation with the ice-covered ocean. This is due to the large contrast in albedo between leads and the surrounding ice. For example, open leads observed by *Pegau and Paulson* [2001] at the Surface Heat Budget of the Arctic Ocean (SHEBA) had an average albedo of 0.066, while J. O. Pinto et al. (Characteristics and atmospheric footprint of springtime arctic leads at SHEBA, submitted to *Journal of Geophysical Research*, 2001, hereinafter referred to as Pinto et al., submitted manuscript, 2001) observed albedos as high as 0.85 over snow covered ice.

[5] During May 1998, the net radiation flux at the SHEBA site in the Beaufort and Chukchi Seas became positive [*Perovich et al.*, 1999a], as the solar radiation began to warm the surface. Surface temperatures increased from $-20°C$ at the beginning of May to between $0°$ and $2°C$ at the end of the month [*Perovich et al.*, 1999b]. During this period, the relatively low albedo of leads, compared to the

---

[1]Now at National Center for Atmospheric Research, Boulder, Colorado, USA.

[2]Now at School of Earth and Atmospheric Sciences, Georgia Institute of Technology, Atlanta, Georgia, USA.

snow covered pack ice, should have an effect on the aggregate surface albedo and thus the absorption of the solar radiation by the ice and ocean.

[6] The intent of this study is to characterize springtime leads in the vicinity of SHEBA. The resulting description of leads can be useful to modelers for evaluating the surface albedo, as well as the dynamics and thermodynamics of the ice pack. The results can also be used to evaluate and interpret satellite determinations of sea ice characteristics using observations from passive microwave radiometers and synthetic aperture radar. The effect of changing sensor resolution (due to differences in aircraft altitude) on the lead statistics is also investigated. The leads were observed by a downward-looking passive microwave radiometer and video camera that were mounted on the underside of the National Science Foundation (NSF)/National Center for Atmospheric Research (NCAR) C-130 during several flights over the SHEBA site in May 1998. In addition, thermal infrared airborne observations from the same aircraft are applied to estimate the ice thickness distribution within leads.

2. Data Description

[7] The SHEBA field experiment took place from October 1997 to October 1998 in the Beaufort and Chukchi Seas [*Perovich et al.*, 1999a]. The Canadian Coast Guard icebreaker *Des Groseilliers* served as a base camp to deploy several instruments on the ice to measure ice, upper ocean, and atmospheric properties in the vicinity of the ship. The primary goals of SHEBA are to determine the ocean-ice-atmosphere processes that affect the ice-albedo and cloud-radiation feedbacks over arctic pack ice, and to improve the parameterization of processes in new and existing models that encompass the Arctic.

[8] Aircraft observations in the vicinity of the *Des Groseilliers* were conducted during April–July 1998 for the FIRE [First ISCCP (International Satellite Cloud Climatology Project) Regional Experiment] Arctic Clouds Experiment [*Curry et al.*, 2000]. This paper utilizes observations obtained from the NCAR C-130 research aircraft.

[9] The Canadian-built Airborne Imaging Microwave Radiometer (AIMR) is a dual-polarization passive microwave scanner operating at 37 and 90 GHz that was mounted on the underside of the C-130 aircraft. The AIMR scans between ±60° across the flight track, so the incidence angle varies across each scan. The specifications and utility of the instrument have been summarized by *Collins et al.* [1996] and *Haggerty and Maslanik* [1996]. The raw data were processed by NCAR's Atmospheric Technology Division (ATD) to correct for aircraft attitude, and to produce vertically and horizontally polarized brightness temperatures for each frequency. This data set also includes brightness temperatures that are produced by averaging the two channels from the AIMR, without applying polarization separation. An example of an image produced from the AIMR during May over the SHEBA area is shown in Figure 1.

[10] Surface skin temperature was acquired using EG&G Heimann Optoelectronics radiation pyrometers [*Laursen*, 1998]. The C-130 deploys model KT 19.85 (hereafter referred to as the KT19), which has a 2° field of view, 0.3 sec response time, and a precision of 1°C. NCAR ATD
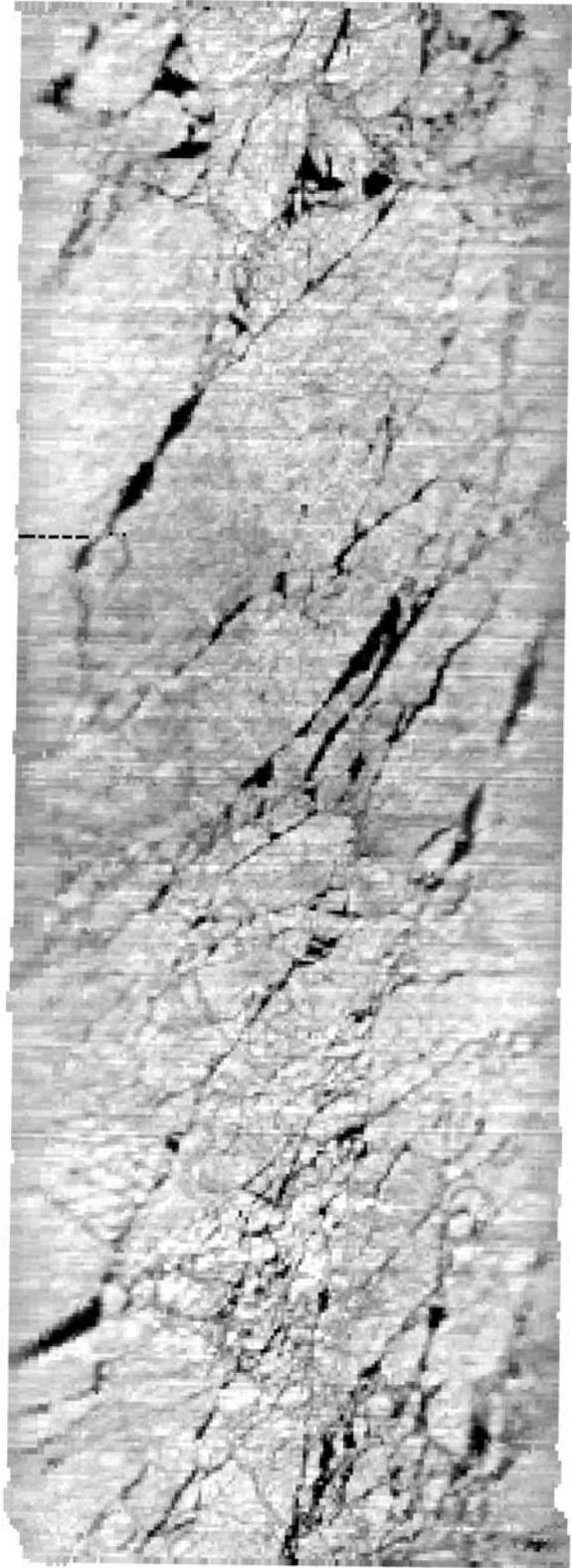

Figure 1. AIMR average brightness temperatures (T_bs) at 90 GHz for 20 May 1998 over SHEBA. Image width is 14 km, aircraft was at an altitude of 4 km and flying east. The ship's position is near the center of the image. T_bs are depicted in gray tones, ranging from 175 K (white) to 250 K (black).
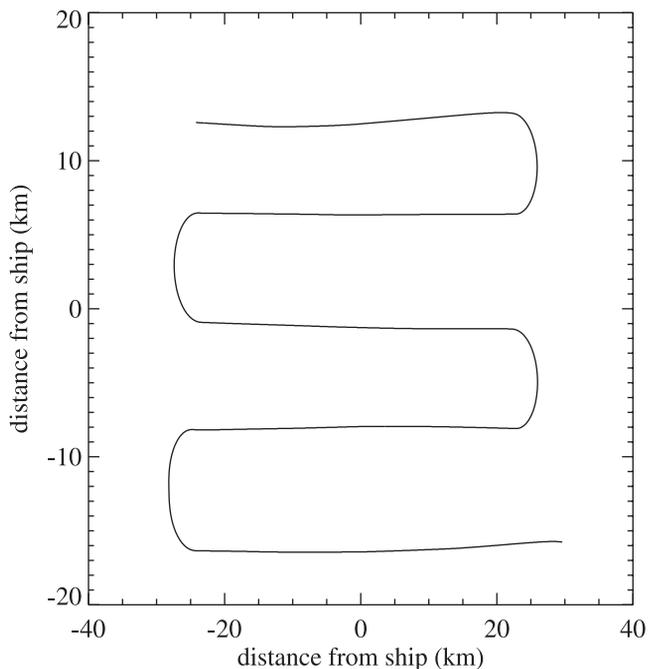
Figure 2. Typical flight pattern for AIMR data acquisition. This pattern was flown at 4.0 km altitude to cover a 50×50 km box.

provided a 5-Hz KT19 data set for this study. A Sony XC-999/999P downward-looking color video camera continuously recorded during each flight. The camera has a 560×745 m field of view and resolution of 1.2 m at an altitude of 700 m.

[11] The C-130 flew eight flights over the vicinity of the SHEBA camp during May 1998. Flight patterns (e.g., Figure 2) were designed and flown to maximize the resolution and spatial coverage of the AIMR, while ensuring continuous scan by the instrument (e.g., an altitude of 1120 m is required for a continuous scan at a typical ground speed of 115 m/s). The patterns provided full coverage of the surface with minimal overlap and are intended to span either a 20×20 or 50×50 km box centered on the *Des Groseilliers*. Seven flight tracks were chosen for analysis, acquired during five days in May (Table 1). Patterns flown at an altitude of ~4 km provide statistics for a 50×50 km box, while the lower-altitude segments span a box that is 20 km on a side. The area covered by each pattern (Table 1) depended on the flight altitude, pattern design, and the maneuverability of the aircraft. AIMR images were constructed from data acquired when the aircraft was flying in an approximate straight and level fashion. Thus there are gaps where the C-130 deviated from straight and level flight.

3. Determination of Refrozen Lead Characteristics

[12] During May, most of the leads were refrozen. Open water in leads is discussed in section 4. Cloudy conditions were prevalent during early May, but did not mask the view of the surface by the AIMR, except for a few small areas. Clear skies prevailed during 20 and 24 May, when a total of four patterns were flown to map the surface. 90 GHz images were analyzed for this study, due to their superior resolution. For example, at 2 km altitude, the 90 GHz resolution is 34 m, but is 90 m at 37 GHz. The resolution of the AIMR determines the minimum lead width represented along each pattern (Table 2). The resolution of the AIMR varied linearly from 25 m at a flight altitude of 1.5 km to 73 m when the altitude was 4.3 km. Note that leads narrower than the resolution of the AIMR can be detected if the lead raises the brightness temperature enough to exceed the threshold.

3.1. Method

[13] Leads with a thin (<40 cm) ice cover were observed to have a particularly high brightness temperature (T_b) at 90 GHz ($T_b > 210$ K) compared to the surrounding multiyear ice ($T_b \sim 180$ K). The elevated brightness temperature of leads with thin ice is due to the higher salinity and resulting larger emissivity in the microwave region of thin ice over multiyear ice [*Eppler et al.*, 1992], as well as to the higher surface temperature of leads compared to thicker ice. The relatively high brightness temperatures permitted identification of refrozen leads within each AIMR image and calculation of various lead statistics for the SHEBA area.

[14] Computer software was written to read, display and analyze each AIMR image. For each image, refrozen leads were identified by manually selecting a point within each lead. The program used a nearest-neighbor approach to record a continuous lead segment by applying a threshold brightness temperature. In some cases, discontinuities were crossed by adding lead segments together, when a similar lead pattern was evident within a few pixels of the lead segment. Once a lead was completely identified within the image, the program computed the lead orientation by applying a line of best fit, which minimized the chi-square error statistic for the group of points. The slope of this line was then adjusted according to the aircraft heading, producing an orientation measured as the angle subtended with the positive *x axis*, increasing in a counterclockwise fashion. Thus, a lead with 135° orientation is aligned along a

Table 1. C-130 Pattern Description, Thin Ice and Open Water Fraction at SHEBA for May 1998

Case	Date (1998)	Altitude, km	Coverage, km^2	Refrozen Leads, %	Open Water, %
A	11 May	2.3	610	8.6	0.40
B	15 May	1.7	389	7.1	0.62
C	18 May	4.3	4007	3.9	0.44
D	20 May	4.0	3064	4.0	1.1
E	20 May	1.5	573	4.2	2.7
F	24 May	4.0	3515	3.9	0.25
G	24 May	1.5	850	4.9	0.75

Table 2. Minimum Detectable Lead Width, Lead Density, Width and Orientation for the Seven Cases in Table 1

Case	Minimum Lead Width, m	Leads/km^2	Lead Width, m	Orientation, degrees
A	39	0.48	169 ± 80	132 ± 23
B	29	0.20	192 ± 77	118 ± 57
C	73	0.087	262 ± 109	126 ± 39
D	68	0.16	241 ± 96	139 ± 16
E	26	1.2	102 ± 44	85 ± 57
F	68	0.13	257 ± 101	134 ± 23
G	26	0.066	126 ± 75	121 ± 34

northwest-southeast axis. Lead orientation is hence specified to be between 0° and 180°.

[15] The average width of the lead was determined next by dividing the number of pixels within the lead (the lead area) by the length of the line of best fit and multiplying by the pixel size. Finally, the program computed a lead fraction for the image by dividing the number of pixels that exceeded the threshold brightness temperature for thin ice by the total number of pixels within the scene. The scene was then redisplayed to highlight the areas identified as thin ice for visual verification. Lead length was not catalogued in this study, as many leads extended beyond the image boundary.

[16] This thresholding method assumed that leads were covered by thin ice, which yielded the increase in brightness temperature as noted earlier. Section 4 discusses the areal fraction of open water, and it was found to be minimal. Mixed pixel effects may have accounted for lead width errors up to the magnitude of the resolution. For example, at an aircraft altitude of 1.5 km, lead width may have been in error by up to 25 m. This estimate assumed that a mixed pixel on each side of the lead may be classified as a lead if it contains at least 50% new ice, which would result in a brightness temperature that would exceed the threshold for lead identification. The error may average out over the ensemble of leads investigated in this study, but is still significant when examining individual leads.

[17] Intervening clouds during the flight patterns before 20 May were observed in some of the AIMR images. Atmospheric water content may affect observed 90 GHz brightness temperatures in the Arctic (e.g., *Haggerty and Curry*, 1999). For example, during some of the 15 and 18 May flights, liquid water paths of 60 gm^{-2} resulted in an increase in brightness temperature of 10–12 K (J. Haggerty, personal communication, 2000). These areas were identified by inspection of the AIMR images, and were excluded from this analysis. These regions accounted for approximately 2% of the area covered during the 11, 15, and 18 May flight patterns.

[18] The penetration depth of dry snow at 90 GHz is a few centimeters [*Eppler et al.*, 1992], and leads with significant snow cover would have surface temperatures similar to the surrounding thicker ice. Therefore, any refrozen leads that were snow covered by more that the penetration depth were not seen by the AIMR and were therefore omitted from this study. However, one of the objectives in this study was to relate the lead fraction to surface albedo, so it was most useful here to omit snow covered leads (or portions of leads), since their albedo does not differ from snow covered pack ice. However, leads that were snow covered by less that the penetration depth were

included in this data set, although their fractional area cannot be determined, since the video camera could not view the surface due to intervening clouds on the earlier flights. The narrow swath of the video camera on the clear-sky flights on 20 and 24 May also prevented complete comparison with the video images. As noted in the next section, no substantial snowfall events occurred during the May study period, so newly formed leads were unlikely to be covered by a significant amount of snow.

3.2. Lead Fraction, Width, and Orientation at SHEBA

[19] Statistics that characterize the individual leads identified from the AIMR images for the May 1998 flights are shown in Tables 1 and 2. Note that the leads used for width and orientation statistics were manually identified for each AIMR image, but the lead fraction was calculated as the percentage of pixels within each image that had a brightness temperature exceeding a determined threshold value. Therefore, the lead (and open water) fraction is computed for each image, while the individual lead statistics (# leads/km^2, width, orientation) are calculated for all leads picked during the manual identification step in the computer program. An effort was made to identify as many leads in each image as possible.

[20] Lead fraction, width and orientation statistics refer to leads (or portions of leads) that were mostly covered with thin ice. The low percentage of open water observed during May (discussed in section 4) indicated that most leads were either completely or mostly covered with ice. To obtain a total lead fraction from Table 1, add the refrozen lead fraction to the open water fraction for each case. The "±" value for the lead width and orientation entries refers to the standard deviation for the set of identified leads, and the first value shown is the mean for each distribution. Lead length is not presented, as many leads identified within the images were segments of larger leads. The large variability of observed leads is evident in the high values of standard deviation for lead width and orientation.

[21] Lead fraction was found to decrease from early to late May at SHEBA, particularly between 15 May and 18 May. During this period, the ice pack within the 50 × 50 km area centered about the ship was converging (Figure 3), as per estimates from the RADARSAT Geophysical Processing System (RGPS) [*Lindsay*, 2002]. The diminished convergence after 18 May may have prevented a further decrease in the lead fraction by 24 May, although other factors also affect the lead fraction. For example, a snowfall that results in a snow depth on a lead that is greater than the penetration depth of the AIMR's 90 GHz channel (a few cm) would result in the lead being undetected by the AIMR. Weather observations (every 6 hours) from the *Des Groseilliers* (*Joint*
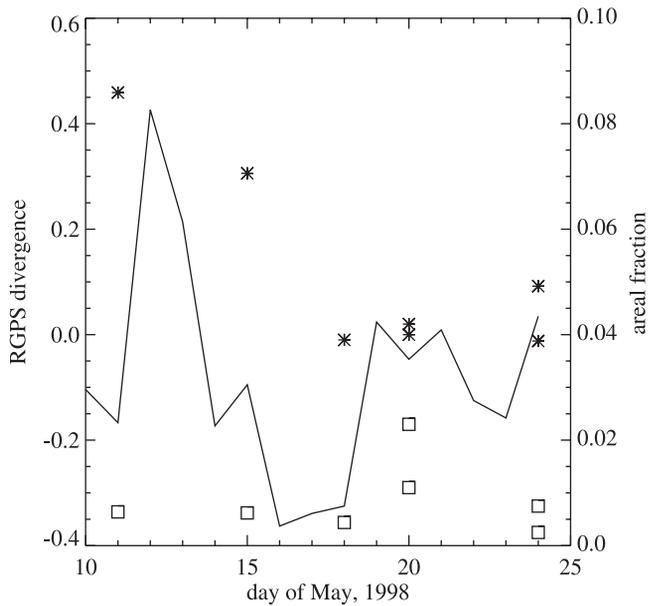
Figure 3. Refrozen lead fraction (*), open water fraction (squares) and RGPS divergence (solid line) from 10 May to 25 May 1998. See Table 1 for details of the lead and open water fractions.

Office for Science Support (JOSS), 2001, available online at http://www.joss.ucar.edu/sheba/catalog) indicated light snow on 12 May and snow on 19 May, but no significant snowfall was observed between 15 May and 18 May, when the largest change in lead fraction was observed. The formation of open water within leads would also result in a decrease in lead fraction (since the lead fraction defined here is for refrozen leads). However, the open water fraction was an order of magnitude smaller that the refrozen lead fraction (as discussed in section 4), so the impact of open water on refrozen lead fraction estimates was minimal.

[22] The altitude of the aircraft also affected the lead fraction determined from the AIMR. The larger lead fraction for case G (Table 1), compared to case *F* (flown on the same day), is due in part to the increased resolution of the AIMR at lower altitudes, although it should be noted that the pattern flown at 1.5 km (case G) covered less area than the pattern flown at 4.0 km altitude (case F). Key et al. [1994] found an exponential decrease in lead fraction with decreasing sensor resolution by degrading Landsat satellite images. This relationship accounts for a portion of the lead fraction decrease observed between 15 and 18 May. However, if one compares the lead fractions between Cases B and E, which were flown at similar altitudes, the lead fraction still decreases to a similar value, implying that the divergence was still an important factor. The lead fractions obtained at SHEBA were similar to the 5% May lead fraction computed by *Lindsay and Rothrock* [1994] from observations during 1975–76 in the Beaufort Sea by *Maykut* [1982]. Their study identified leads as containing a combination of thin ice and open water.

[23] The number of leads per km^2 (or lead occurrence) is presented in Table 2. The leads represented in this category were those that were manually identified within each AIMR image and subsequently processed by the lead algorithm.

There is no observed relationship between these data and aircraft altitude, and no trend is apparent in this statistic through May.

[24] Lead width histograms are shown in Figure 4. In general, smaller leads were observed most often, although leads that were below the AIMR resolution may not have been detected. The dominance of small leads is consistent with submarine sonar observations [e.g., *McLaren*, 1989] and was also observed by *Steffen* [1987] during aircraft transects over Lancaster Sound, Baffin Bay and the North Water area during winter 1980/1981. The disappearance of smaller leads with decreasing sensor resolution noted by *Key et al.* [1993] is evident in Figure 4, as the peak of the width histogram shifted toward wider leads with increasing aircraft altitudes (e.g., 4 C, D, and F).

[25] The mean lead widths were narrower than widths observed by *Lindsay and Rothrock* [1995], who estimated lead widths from advanced very high resolution radiometer (AVHRR) observations. This discrepancy is mostly due to the difference in resolution between satellite and aircraft observations. In this study, only a few leads were observed with a mean width greater than 400 m, and leads as narrow as 25 m were detected by the AIMR at an altitude of 1.5 km. *Lindsay and Rothrock* [1995] found that the AVHRR detected leads as narrow as 1 km, which is wider than the widest lead observed in this study.

[26] The variability in lead width distribution obtained using the AIMR 90 GHz observations was primarily a function of the resolution of the AIMR, as mean widths increased with increasing flight altitude (i.e., decreasing resolution) in an approximately linear fashion (Figure 5). The slope of the fitted line was about 0.46, which indicates the increase in mean lead width (m) per each meter of additional flight altitude. This relationship is also evident in Table 2, as the larger average lead widths were observed at the higher aircraft altitudes (i.e., smaller AIMR resolutions).

[27] The influence of sensor resolution on the observed lead width and orientation distribution has been discussed by *Key et al.* [1994, 1993]. They found that larger leads tend to "grow" with decreasing sensor resolution, while smaller leads disappear. The resulting change in mean lead width could be significant for modeled estimates of turbulent heat fluxes [e.g., *Maslanik and Key*, 1995]. To compensate for the exclusion of smaller leads that were undetectable in the AIMR data, observations from a downward-looking video camera were merged with the passive microwave data to produce a lead width distribution that includes narrow leads.

[28] The downward-looking video camera on the C-130 permitted a high-resolution view of lead widths at SHEBA, including leads that were only a few meters wide. On 24 May, a pattern similar to the typical AIMR pattern (Figure 2) was flown at 700 m altitude for the purpose of video acquisition. The video was analyzed to obtain lead widths along this pattern, which covered 139 km^2. The resulting lead width distribution was combined with the distribution derived from the AIMR analysis from the pattern flown at 4 km altitude during the same day. The distributions were combined by factoring in the difference in areal coverage between the two flight patterns, producing a histogram of the fractional coverage of leads versus lead width for the 50 × 50 km box centered about the ship on 24 May (Figure 6).
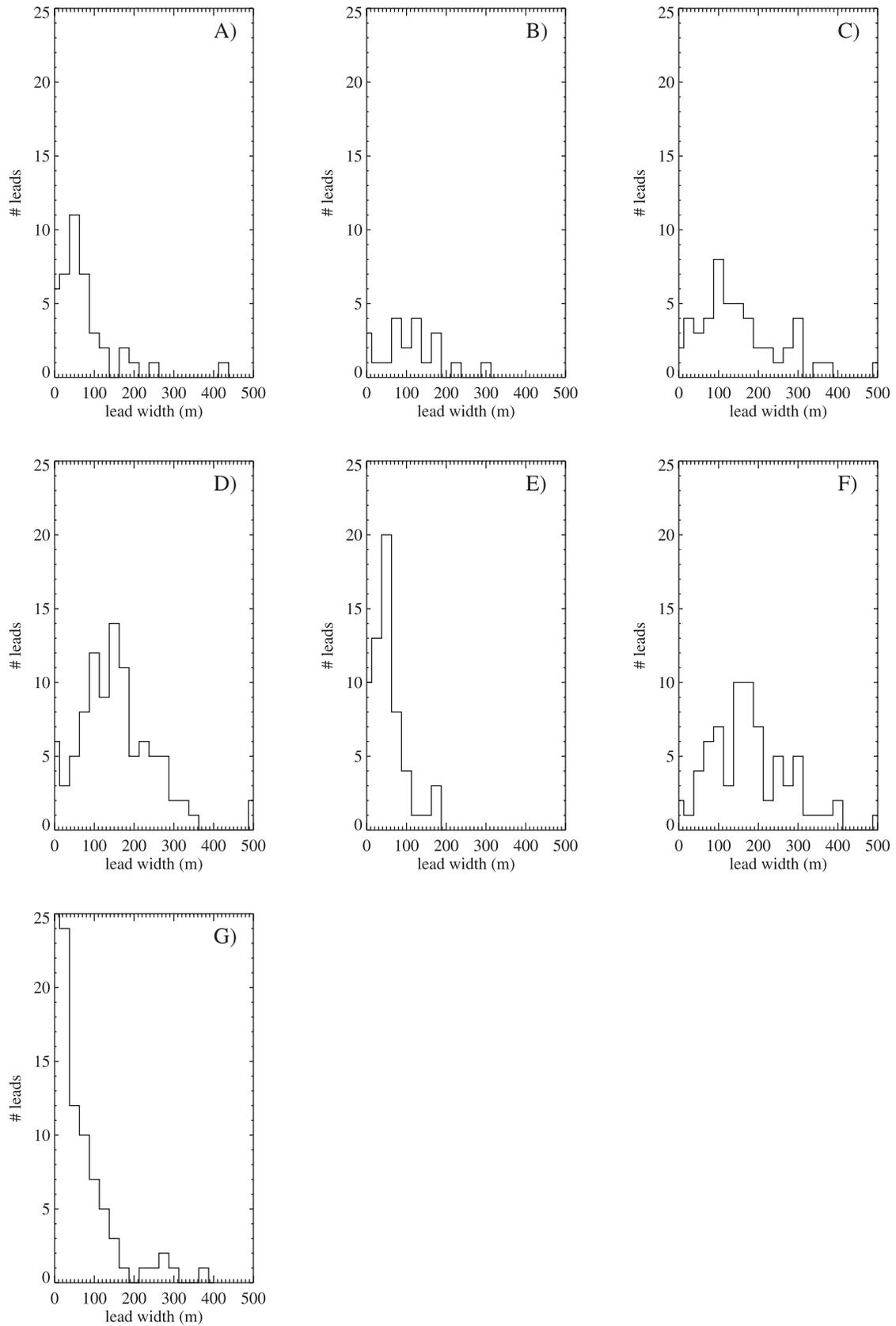
Figure 4. Lead width histograms for AIMR patterns: A) 11 May, alt = 2.3 km; B) 15 May, alt = 1.7 km; C) 18 May, alt = 4.3 km; D) 20 May, alt = 4.0 km; E) 20 May, alt = 1.5 km; F) 24 May, alt = 4.0 km; G) 24 May, alt = 1.5 km.
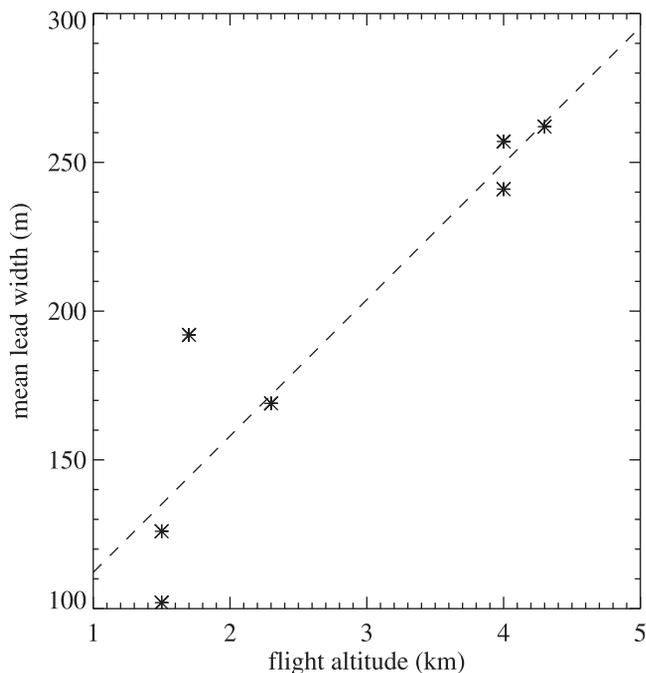
Figure 5. Mean lead width versus aircraft altitude.

The distribution is approximated (dashed curve) according to:

$$f = e^{-2.15 - 0.014w}, \tag{1}$$

where f is the lead fraction for each width w (m). For example, the fraction (f) of leads 50 m wide is approximated by (1) as 0.0578, or 5.78%. This distribution is dominated by leads narrower than 100 m, which account for 75% of the lead fraction.

[29] The width distribution (1) describes all leads that were observed within the 50 × 50 km box at SHEBA on 24 May that were at least 1 m wide. *Lindsay and Rothrock* [1995] also found this type of relationship, although the leads categorized in their study were observed from satellite, and were therefore much wider (>1 km). Such a negative exponential distribution appears typical of lead width distributions in general [*Key and Peckham*, 1993].

[30] Individual lead width and orientation are shown in Table 2 and plotted in Figure 7. Each point in the figure represents a single lead. Note that the orientation is defined by the positive angle subtended with the *x axis* (which points east). Thus, a lead with an orientation of 135° is aligned along a northwest-to-southeast line. Since the orientation is specified to be between 0° and 180°, a lead with an orientation of 179° is only 2° different than a lead with a 1° orientation. Each plot represents the statistics acquired along the pattern (e.g., Figure 2) on the indicated day and altitude.

[31] The majority of leads observed during May in the vicinity of the SHEBA camp had an orientation in a northwesterly (i.e., along a northwest to southeast line) direction (Figure 7 and Table 2). This orientation preference is also observed in a high-resolution visible-band satellite image over SHEBA obtained on 17 May (*National Snow and Ice*

Data Center, 2000, digital data available from nsidc.org, Boulder CO) and a 20 May visible-band image from the MODIS Airborne Simulator that was flown over the SHEBA area aboard the NASA ER-2 [*Beitzel and Young*, 2000] (also available online at ltpwww.gsfc.nasa.gov/MAS/doc_new.html). Interestingly, *Miles and Barry* [1998] found that the mean lead orientation for the winters of 1979–1985 (except 1980–1981, which was not included in their study) was also characterized by a northwestern orientation in this region of the Arctic and may reflect the prevailing wind patterns in this area. Leads tend to orient perpendicular to the prevailing wind direction [*Miles and Barry*, 1998], and NCEP Reanalysis sea level pressures for this area of the Arctic for the days in Table 1 indicate a prevailing wind out of the northeast, which is approximately normal to the mean lead orientation (except for case E). The mean orientation of leads also is consistent with the circulation of the Beaufort Gyre.

[32] These lead orientations and the diamond-shape arrangement of leads are characteristic of the Beaufort Sea ice pack [*Marko and Thomson*, 1975, 1977] and have been shown to be related to the dominant wind and deformation patterns in the area [*Overland et al.*, 1992; *Walter and Overland*, 1993]. Those studies noted that the intersection of the large leads occurs at about a 30° angle, and that there is a general fractal nature to the lead arrangements such that patterns persist at different scales. Our results support these earlier findings, suggesting that the basic ice conditions and forces controlling the lead patterns remain similar over the past 30 years. These results also suggest that the lead patterns aren't particularly sensitive to ice thickness, given that the thickness was considerably below average during the SHEBA period.

[33] Lead systems observed from the C-130 flight altitudes had complex patterns. Many leads exhibited multiple
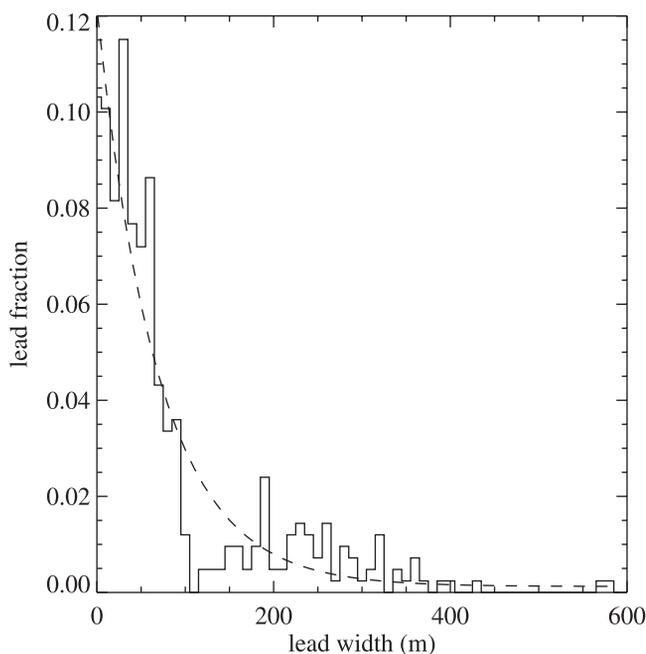

Figure 6. Lead width histogram for 24 May 1998 in the 50 × 50 km box centered on the ship, as derived from AIMR and video observations.
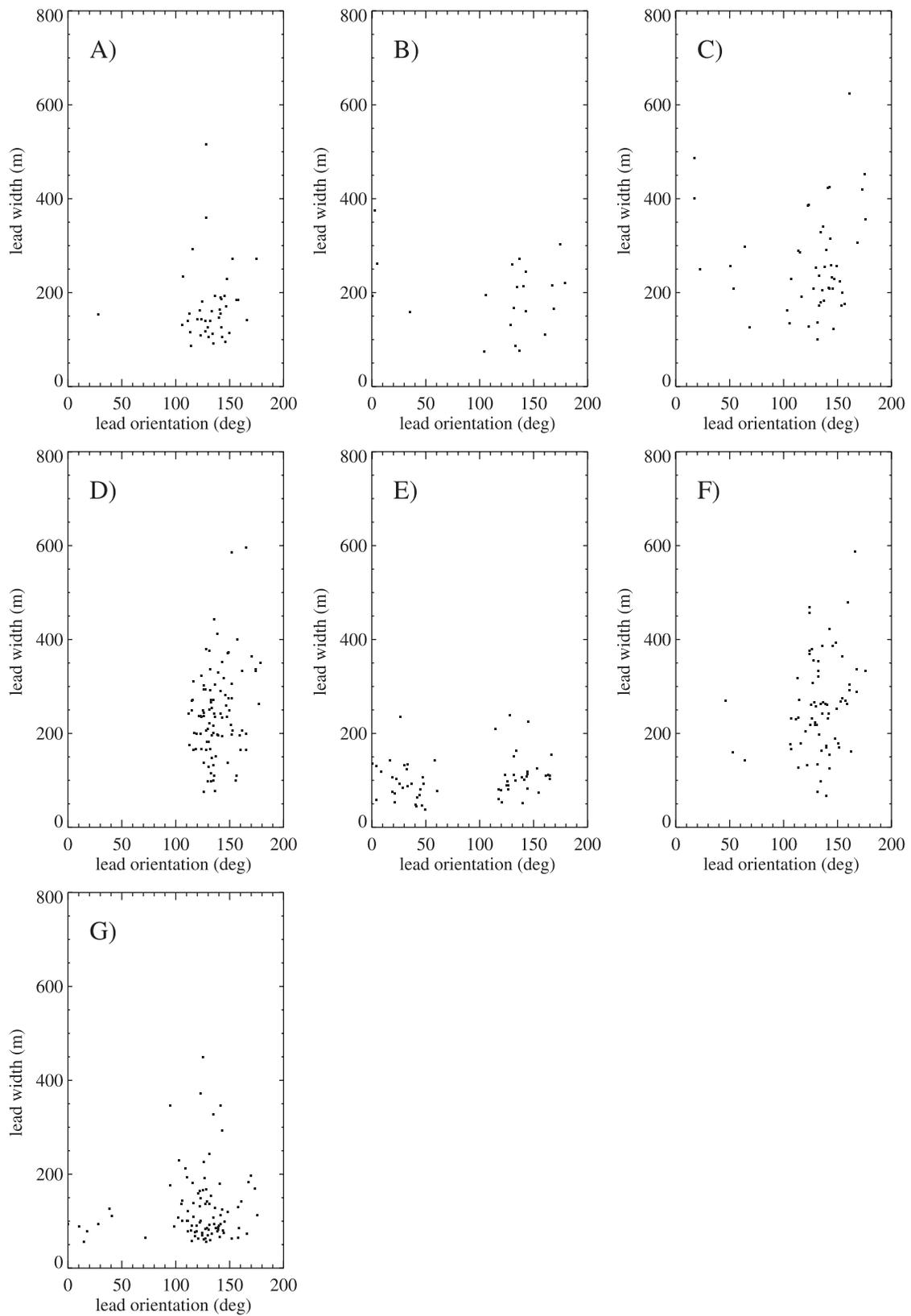
Figure 7. Lead width versus orientation for the same patterns shown in Figure 4.

bifurcations and irregularities along the perimeter. The increasing diversity of lead orientation at lower aircraft altitude is evident in Table 2, as the largest orientation standard deviation was found for two patterns at low aircraft altitudes. There is also a dramatic difference between the mean orientation for cases D and E, which is due in part to the lower-altitude detection of secondary fractures that are aligned at an angle to the wider leads (also see Figures 7d and 7e). *Key et al.* [1993] noted a shift in orientation distribution with the change in pixel size using Landsat observations.

4. Determination of Open Water Fraction

[34] Field observations during May at SHEBA confirmed that there were leads with open water in the vicinity of the ship [*Perovich et al.*, 1999b], although the areal coverage appeared to be very small while observing the surface from the C-130. However, even a small amount of open water may have a discernable impact on the surface albedo, surface sensible heat flux, and the penetration of shortwave radiation into the upper ocean. We therefore applied further analysis to extract information about the occurrence of open water within the SHEBA area.

4.1. Method

[35] A polarization ratio (PR) applied to the AIMR 37 GHz observations was used to calculate ice concentrations. *PR* is defined as:

$$PR = (37V - 37H)/(37V + 37H) \qquad (2)$$

where $37V$ and $37H$ are the 37 GHz brightness temperatures for vertical and horizontal polarizations, respectively. *PR* capitalizes on the large polarization difference between ice and open water, and provides the basis for determining the fractional coverage of ice and open water within individual footprints. *PR* is used similarly within the NASA Team Algorithm, which is applied operationally to SMMR and SSM/I data [*Cavalieri et al.*, 1984]. A benefit of using *PR* rather than a single channel is that the normalized-difference ratio reduces the dependence of brightness temperature on the physical temperature of the surface [*Steffen et al.*, 1992], which may vary spatially and temporally in polar regions.

[36] Microwave emissivity of various ice types and open water has been catalogued by *Eppler et al.* [1992]. These values were obtained from satellite and laboratory observations of sea ice at incidence angles of approximately 50°, which permitted separate detection of the horizontally and vertically polarized portions of the 37 GHz signal. The published emissivities were used to calculate *PR* tie points for 100% open water and 100% thick ice using (2) in a procedure to determine the fraction of open water in each AIMR image produced from C-130 observations over SHEBA during the FIRE-ACE campaign in May 1998. The *PR* difference between first-year and multiyear ice was not taken into account, as the concentration of each ice type has not been determined. Use of a spectral gradient to determine ice type as is done in the NASA Team Algorithm yielded ambiguous results given that an ice type-dependent gradient between the available 90 GHz and 37 GHz channels on the AIMR is less effective at discriminating

these ice types than is the 37 GHz versus 19 GHz gradient used by the NASA Team Algorithm for SSM/I data. This lack of discrimination between first-year and multiyear ice did not lead to a large error in the analysis.

[37] The *PR* for first-year ice is 0.023, for multiyear ice 0.040, and 0.256 for open water. Thus the difference in *PR* between first-year and multiyear ice is only 8% of the difference between multiyear ice and open water. Given the *PR* tie points for 100% thick ice and 100% open water, a linear mixing calculation was then used to calculate the fraction of thick ice (i.e., ice concentration) and open water within a pixel, based on the observed *PR* value for that pixel. For example, suppose the *PR* computed for an AIMR image pixel in a strip is 0.062. The algorithm would then assign a makeup of 10% open water and 90% ice (0.1 * 0.256 + 0.9 * 0.040) to this pixel. Very thin ice affects the retrieval by appearing as some smaller fraction of open water. At 37 GHz, however, the effects on the analysis here were minor.

[38] Two narrow (2 pixel) strips, centered about the portion of the AIMR scan that viewed the surface at a 50° incidence angle, were analyzed for each 37 GHz AIMR image obtained during specialized AIMR patterns flown in May. *PR* was determined for each pixel within the two strips and converted to ice concentration for that pixel as described above. The fractional coverage of open water for each pixel is averaged along the two strips, and an open water percentage is computed for each image. Open water fractions for each case in May (Table 1) are then determined by weighting each image according to its along-track coverage (this distance varies from image to image).

4.2. Open Water Fraction at SHEBA

[39] The open water fraction at SHEBA during May, derived from the AIMR's 37 GHz observations, is shown in Table 1 and Figure 3. Figure 3 also depicts the RGPS divergence that was observed during the period of open water measurements, as well as the refrozen lead fraction.

[40] The areal fraction of open water remained below 1% during the 5 days of May observation, with the exception of 20 May when the open water percentage rose to 1–2%. This increase followed the end of a convergence event, as evidenced by the RGPS data. One, however, would expect the open water fraction to decrease during convergence, and then remain the same after the conclusion of this event, if the ice motion was responsible for the change in open water fraction. The wind speed on 20 May was 7 m/s [*JOSS*, 2001], which may have caused some localized divergence that was not detected by the course resolution of the RGPS system.

[41] Open water fraction decreased between 20 and 24 May, which may be due in part to the growth of thin ice within leads, since temperatures observed at the ship [*JOSS*, 2001] were as low as −14°C. There was also a minor convergence event between 20 and 24 May, which contributed to the decline in open water.

[42] On 20 and 24 May, the open water fraction was significantly higher during the low-altitude (1.5 km) patterns than the 4-km altitude patterns. The correlation between aircraft altitude and open water fraction, however, is weakly negative (R = −0.46), and the use of the mixed-pixel *PR* algorithm should not be dependent directly on sensor resolution. The difference is observed open water
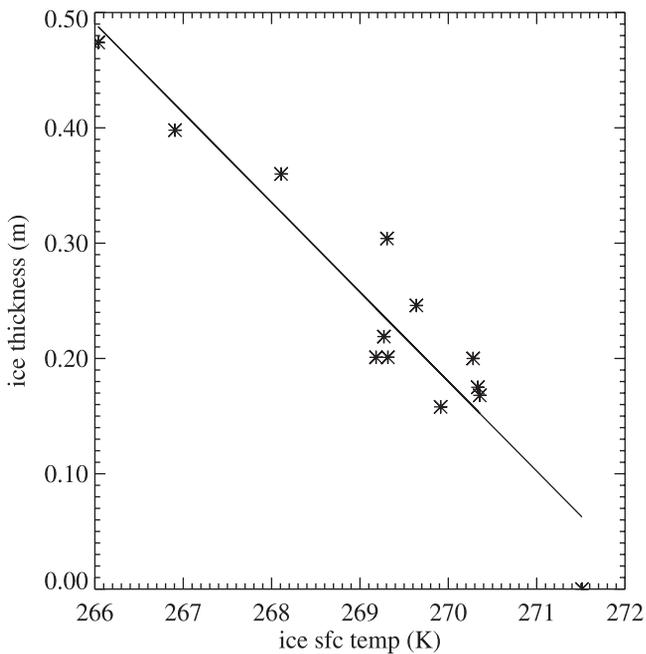
Figure 8. Ice thickness versus ice surface temperature on 24 May (2300 UTC), derived from the *Schramm et al.* [1997] ice model using forcings from SHEBA surface observations. Model computations (*) and the best linear fit are shown.

fraction between flight altitudes is more likely due to the differing coverage of each pattern: the lower-altitude patterns covered a 25 × 25 km box, while the 4-km runs were designed to observe a 50 × 50 km box, with each box centered about the *Des Groseilliers*.

5. Derivation of Ice Thickness Within Leads

[43] Estimation of the skin temperature within leads using KT19 observations has been applied to determine the ice thickness distribution over the leads. A relationship between the ice surface temperature and ice thickness at SHEBA was derived using a single-column ice thickness distribution model [*Schramm et al.*, 1997]. The model is forced using SHEBA observations of precipitation, downwelling shortwave and longwave fluxes, and surface air temperature, humidity, and winds [*Curry et al.*, 2001]. The sea ice temperature and thickness are computed by balancing the heat fluxes at the ocean-ice and ice-atmosphere interface. At 2300 on 24 May, during the pattern flown at 700 m altitude for video acquisition, the model computed ice thickness (h, in m) and ice surface temperature (T_{sfc}, in K) as shown in Figure 8. An approximate relationship (dashed line) between new ice thickness and ice surface temperature for this date is:

$$h = 21.15 - 0.07766\ T_{sfc}. \qquad (3)$$

[44] Next, the KT19 observations for the video pattern were adjusted to account for emission and absorption of infrared radiation in the atmosphere. This correction was determined by applying a radiative transfer model to KT19

observations at SHEBA [*Haggerty and Curry*, 2001]. The correction was found to be:

$$T_{sfc} = T_{KT19} + \Delta T, \qquad (4)$$

where

$$\Delta T = 0.187\ T_{KT19} - 50.4$$

[45] In this study, "thin" ice was defined as having a thickness less than 40 cm. Using Figure 8, this translates to an ice surface temperature of at least 267 K. All corrected surface temperatures (T_{sfc}) above 267 K are used in (4), yielding an ice thickness distribution within the leads (Figure 9). The ice thickness distribution can be approximated (dashed line) according to:

$$g(h) = 21.6 - e^{3.51 - 0.0212h}, \qquad (5)$$

where $g(h)$ is the percentage of ice within the observed leads with a thickness h (cm). The thin ice fraction derived using the corrected KT19 observations and the *Schramm et al.* [1997] sea ice model infer that leads were covered with ice that was at least 20 cm thick. The footprint of the KT19 at an altitude of 700 m is ~25 m, so it is quite possible that thinner ice and open water were part of the KT19 footprint in some cases. The ability of the KT19 to obtain an observation completely within a lead, as well as the heterogeneity of ice thickness within the 25 m KT19 footprint, are sources of error for deriving lead ice thickness using this technique.

6. Surface Albedo and Lead Width from AVHRR Observations

[46] Airborne passive microwave and video observations have been combined to produce a characterization of lead
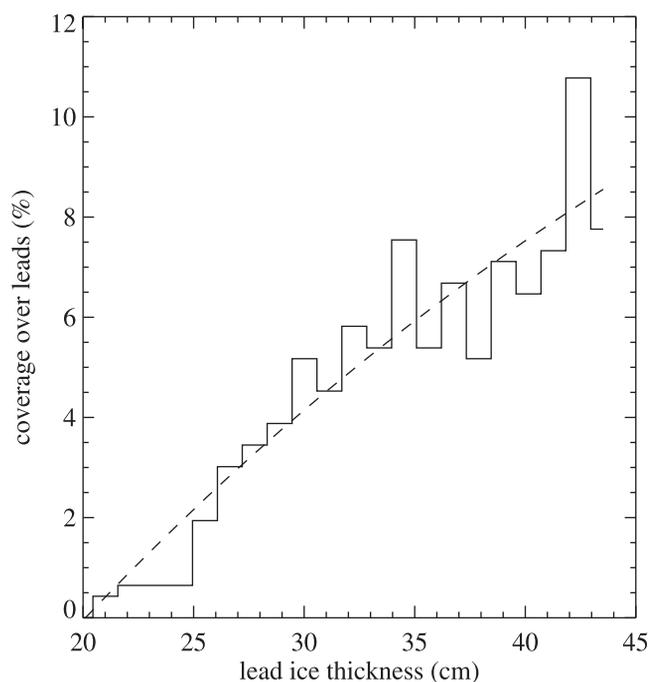

Figure 9. Thin ice thickness within 25-m footprints for 24 May using corrected KT19 surface temperatures and the relationship in Figure 8.
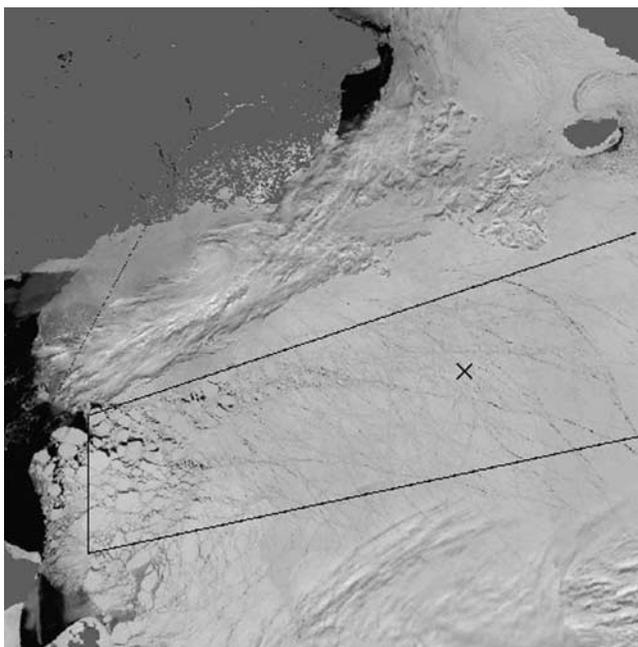
Figure 10. AVHRR albedo image for 24 May 1998. Alaska is in the upper left, Russian coast and island of G Sovetskaya in upper right. North is approximately to the lower right. Position of the ship is marked by X. Image size is 1630 km × 1602 km. The study area is outlined. The straight line in the left center of the image is a processing artifact.

width in the vicinity of SHEBA (section 3.2). To put these aircraft observations into a broader perspective, satellite albedo data are utilized to summarize the spatial variability in albedo and lead characteristics in the SHEBA region and the Western Arctic during late May 1998. At this time, uncertainties in albedos obtained by the C-130 remain to be resolved, so those data are not analyzed here.

[47] The comparatively low albedo of open water and thin ice, compared to snow covered ice, impacts the aggregate surface albedo. For example, open lead surface albedo at SHEBA was 0.066 under cloudy conditions during the summer [*Pegau and Paulson*, 2001]. Pinto et al. (submitted manuscript, 2001) measured an albedo of 0.08 for ice between 1 and 3 cm thick over a lead during late April near the *Des Groseilliers*. Over snow covered ice, *Perovich et al.* [1999b] observed albedos of 0.80 to 0.83 along the albedo line on 25 May.

[48] The large contrast in albedo between open water/thin ice and snow covered ice during May at SHEBA permits a characterization of leads from albedo observations. Imagery acquired by the Advanced Very High Resolution Radiometer (AVHRR) on the NOAA polar orbiting satellites provide albedo estimates over large areas, and are used here to estimate lead coverage for comparison to the aircraft-measured lead information near the SHEBA ship. The AVHRR data used are part of the AVHRR Polar Pathfinder (APP) data set [*Maslanik et al.*, 2001] [*Hutchinson and Scambos*, 1997; *Maslanik et al.*, 1998] archived by the National Snow and Ice Data Center [*Scambos et al.*, 2001, data available on digital media, nsidc.org], with subsets for

the SHEBA region available from the JOSS archive [*JOSS*, 2001]. These APP data consist of twice-daily composited, georeferenced and calibrated radiances and atmospherically corrected clear-sky broadband albedo and skin temperature at grid resolutions of 1.25 km and 5 km. The 1.25 km APP products were used here. See *Maslanik et al.* [2001] and *Scambos et al.* [2001] for a description of the derivation of these data.

[49] Aggregation of these 1.25 km albedo values produced an image for the region (Figure 10) that shows the derived surface albedo on 24 May at 1400 UTC. A land mask is applied to the image and areas of cloud are visually identified. A cloud-free region over the ice pack is identified (shown in Figure 10) for further analysis. This region has mean dimensions of 1459 km × 436 km.

[50] Albedos within this region were found to vary from 0.08 in open water areas to 0.80 over snow covered ice. The most prevalent albedos in this region are shown in Figure 11. An AVHRR albedo of 75% is most commonly observed in the region. The AVHRR albedo in the 1.25 km pixel containing the *Des Groseilliers* (marked by *X* in Figure 10) was 77.8%, which is somewhat higher than the mode of Figure 11, but is nonetheless not uncommon. The 80–83% albedos found along the 200 m albedo line [*Perovich et al.*, 1999b] were higher than most of the AVHRR albedos. *Stroeve et al.* [2001] suggest that the APP albedos have a small negative bias, which may account for the slightly lower values for snow covered ice compared to those observed in the field at SHEBA. The SHEBA albedo line measured albedos over snow covered ice only, while the large AVHRR pixel may include this surface type as well as thin ice, open water, and additional effects such as shadows from ridges.

[51] By noting that the north is approximately toward the lower right of Figure 10, one can observe a general north-
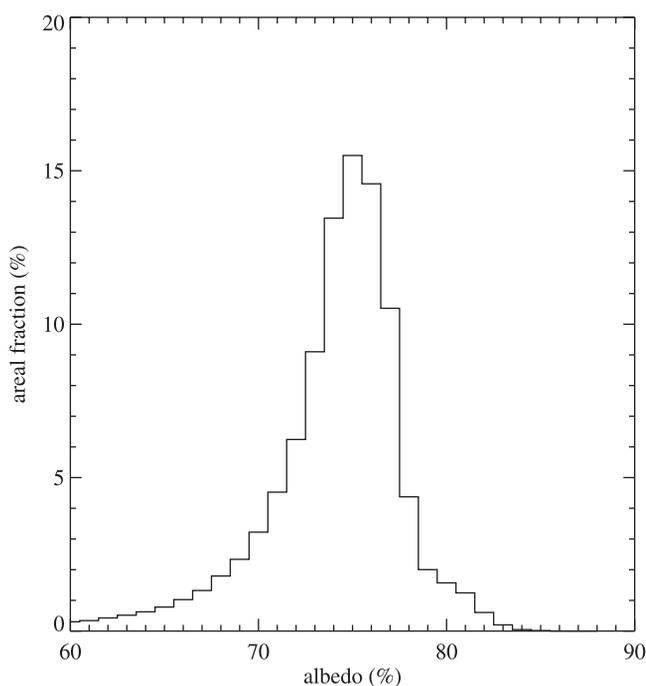

Figure 11. AVHRR albedo histogram for the study area shown in Figure 10.

westerly orientation of the major leads, as was found from the passive microwave observations in this study. Large-scale lead patterns are diamond-shaped, as have been previously observed in the Arctic by *Lindsay and Rothrock* [1995] and *Miles and Barry* [1998] (also see discussion in section 3.2).

[52]   The albedos within the 50 × 50 km box centered by the *Des Groseilliers* were extracted from the AVHRR image, contoured, and are shown in Figure 12. In this region, albedos determined from AVHRR varied from 45.7% to 79.5%, due primarily to the fraction of open water and/or thin ice found within each pixel. Interestingly, the areas of lower albedo are roughly aligned in a northwesterly direction, presumably due to the influence of leads in the region with this orientation. The mean albedo of this area was 74.8%, which is significantly lower than the albedo in the AVHRR pixel containing the SHEBA area (77.8%).

[53]   By combining airborne video and passive micro-wave observations of the surface, an exponential decrease in lead fraction with increasing width was found (see section 3.2 and Figure 6). A second method to derive a lead width distribution for the same region and day utilizes the AVHRR albedo observations. The albedo within each 1.25 km pixel (α) viewed by this sensor is a result of the linear combination of the individual albedos (α_i):

$$\alpha = \Sigma A_i \alpha_i, \qquad (6)$$

where A_i is the areal fraction of each surface type within the pixel. A_i is found from (6), by noting that $\Sigma A_i = 1$ and by assuming that only snow covered ice and open water/thin ice occurred on the surface. During May, these were the predominant surface types found by SHEBA investigators [e.g., *Perovich et al.*, 1999a].

[54]   Using an albedo of 0.08 for open water/thin ice and 0.78 for snow covered ice, (6) is applied to derive the areal fraction of leads within each pixel. The lead fraction is multiplied by 1.25 km (the AVHRR pixel size) to compute a
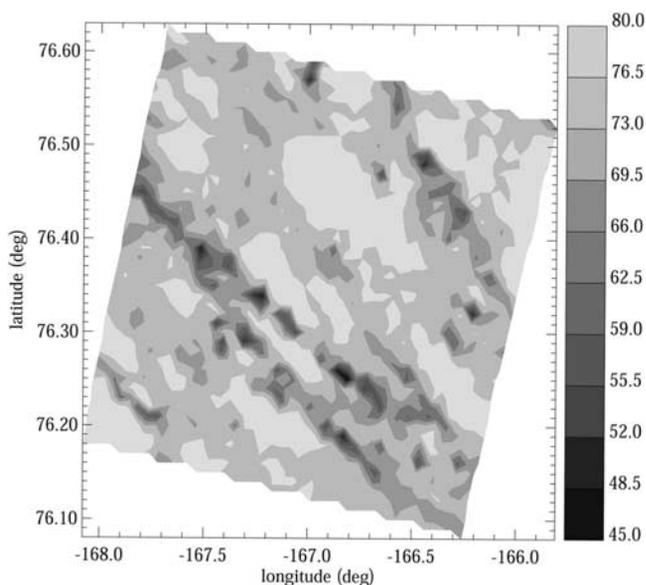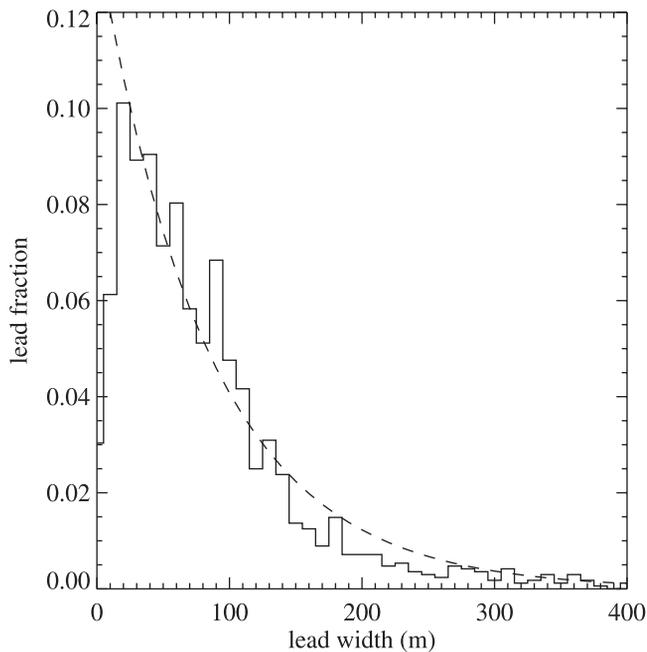

Figure 13.   Lead width distribution derived from AVHRR albedos.

lead width for each pixel. The lead width derived using this method may combine 2 or more leads within a pixel, having a total width equal to the single lead width that is computed. There is no identification of lead shape within the pixel, so in some cases a lead may actually be an area composed of broken ice and water, rather than a typical rectilinear-shaped lead.

[55]   The resulting lead width distributions are shown for the entire region (Figure 13) and for the 50 × 50 km box

Figure 12.   Contoured albedo (%) over the 50 × 50 km box centered on the ship.
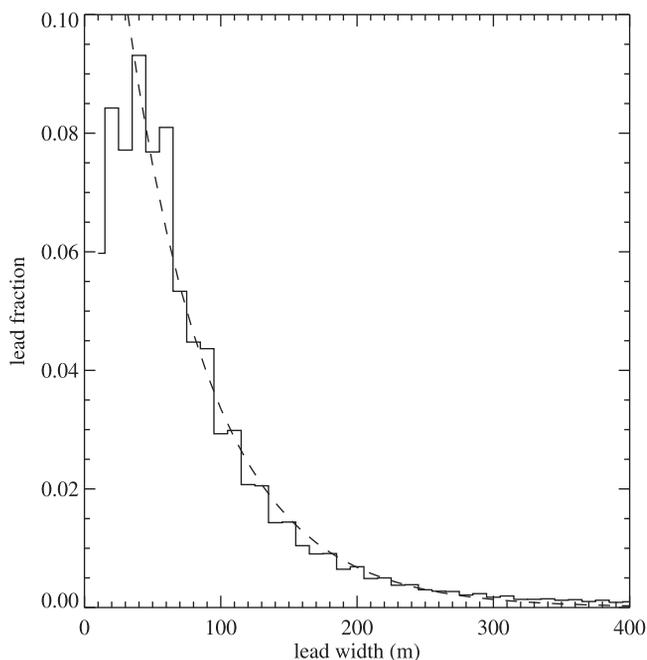

Figure 14.   Lead width distribution derived from AVHRR albedos (50 × 50 km box).

(Figure 14). Approximate lead width distributions (dashed curves in each figure) are given by:

$$f = e^{-1.96-0.016w} \qquad (7)$$

for the entire region and

$$f = e^{-2.00-0.012w} \qquad (8)$$

for the 50 × 50 km box, with f the lead fraction (%) for a particular width w (m).

[56] The exponential lead width distributions defined by (7) and (8) are similar to relationship (1), and leads narrower than 150 m are most prevalent. The number of leads computed from AVHRR observations falls off for leads narrower than about 20 m, in contrast to the distribution given by (1). The effect of these narrow leads on the aggregate albedo is probably too small to be detectable within the radiometric resolution of the AVHRR. The narrow leads included in (1) were observed by the airborne video camera, which detected leads as narrow as 1 m.

[57] The similarity between the lead orientation and lead width distributions in the SHEBA area (derived from both methods) and the Western Arctic region identified in this study suggests that the lead characteristics in the SHEBA area were representative for the region as a whole. The form (i.e., negative exponential) of the relationships described by (7) and (8) were also observed in the Western Arctic in spring by *Lindsay and Rothrock* [1995] and *Maslanik and Key* [1995], which implies that these lead width distributions are typical for this season and region.

7. Summary

[58] Airborne passive microwave observations were used to characterize ice-covered leads at SHEBA during May 1998. The leads in this area were mostly covered with thin ice, as open water fraction was an order of magnitude lower than thin ice fraction. The refrozen lead fraction decreased in the latter half of May, which was associated with local convergence of the pack ice, as determined from RADAR-SAT ice deformation observations.

[59] Refrozen leads detected by the AIMR had widths ranging from the resolution of the instrument (e.g., 25 m when the aircraft was at 1.5 km altitude) to nearly half a kilometer. The mean width viewed by the AIMR increased with the decreasing spatial resolution of the imagery, as found by *Key et al.* [1993]. A cumulative lead width distribution is obtained by combining the AIMR and lower-altitude video observations. Leads narrower than 100 m accounted for 75% of this distribution.

[60] The majority of leads were oriented in a northwesterly direction. This information can be combined with wind direction and wind speed to determine fetch in the SHEBA vicinity. A technique to obtain open water fraction utilizing the AIMR's 37 GHz observations is presented. Open water fraction increased from about half a percent in early May to 1–2% on 20 May.

[61] By applying the relationship between ice surface temperature and ice thickness computed by a sea ice model, the ice thickness over leads at SHEBA is inferred from airborne thermal infrared observations. Using this technique, the mean thin ice thickness within a 25-m footprint was estimated to be at least 20 cm thick.

[62] The spatial variability of surface albedo in late May within the SHEBA region and in the Western Arctic is examined using AVHRR albedo observations. The average albedo in the SHEBA region (74.8%) is lower than the albedo for the 1.25-km AVHRR pixel containing the ship (77.8%) and the albedo observed over the 200 m albedo line the next day (80–83%) by *Perovich et al.* [1999b]. However, the SHEBA region albedo is representative of the Western Arctic on this day, as the most commonly observed AVHRR albedo was about 75%.

[63] Lead width distributions are derived from the AVHRR albedo data and show a preference for narrow (30–50 m wide) leads, with an exponential decrease in lead fraction with increasing lead width. This type of relationship is observed for the SHEBA region, as well as the Western Arctic, and has been found by others in previous years. Northwesterly lead orientation is found by inspection of the AVHRR albedo image for 24 May and was observed by the airborne passive microwave sensor utilized during FIRE/SHEBA, which also implies that this lead statistic in the SHEBA region is representative of the Western Arctic during late May 1998.

[64] The lead statistics derived in this study should be useful in developing and testing parameterizations for climate modelers. These data will also help in further quantifying the accuracy of lead statistics calculated from different remote sensing data sets.

References

Beitzel, T., and S. Young, FIRE III Arctic Cloud Experiment field mission report, 2000.

Cavalieri, D. J., P. Gloersen, and W. J. Campbell, Determination of sea ice parameters with the NIMBUS-7 SMMR, *J. Geophys. Res.*, *89*, 5335–5344, 1984.

Collins, M. J., F. G. R. Warren, and J. L. Paul, Airborne imaging microwave radiometer, Part I, Radiometric analysis, *IEEE Trans. Geosci. Remote. Sens.*, *34*, 643–655, 1996.

Curry, J. A., P. V. Hobbs, M. D. King, D. A. Randall, and P. Minnis, et al., FIRE Arctic Clouds Experiment, *Bull. Am. Meteorol. Soc.*, *81*(1), 5–29, 2000.

Curry, J. A., J. L. Schramm, D. K. Perovich, and J. O. Pinto, Applications of SHEBA/FIRE data to evaluation of snow/ice albedo parameterizations, *J. Geophys. Res.*, *106*(D14), 2001.

Eppler, D. T., et al., Passive microwave signatures of sea ice, in *Microwave Remote Sensing of Sea Ice*, edited by F. D. Carsey, 1992.

Haggerty, J. A., and J. A. Curry, Retrieval of arctic cloud properties from an airborne microwave radiometer, in *Proc., Fifth Conf. on Polar Met, Am. Meteorol. Soc.*, 97–102, 1999.

Haggerty, J. A., and J. A. Curry, Variability of sea ice emissivity estimated from airborne passive microwave measurements during FIRE-SHEBA, *J. Geophys. Res.*, *106*(D14), 2001.

Haggerty, J. A., and J. A. Maslanik, Airborne Imaging Microwave Radiometer measurements of sea ice during the Beaufort Arctic Storms Experiment, in *Second Int. Airborne Remote Sens. Conf., San Francisco, CA, 24–27 June, II*, 501–506, 1996.

Hutchinson, T. A., and T. A. Scambos, High-resolution polar climate parameters derived from 1-km AVHRR data, in *Proc. of the Eighth Symp. on Global Clim. Change Stud., Am. Meteorol. Soc.*, Long Beach, CA., 284–289, 1997.

Joint Office for Science Support, *SHEBA Field Catalog, land-based version*, 2001.

Key, J., and S. Peckham, Probable errors in width distributions of sea ice leads measured along a transect, *J. Geophys. Res.*, *96*, 18,417–18,423, 1993.

Key, J., R. Stone, J. Maslanik, and E. Ellefsen, The detectability of sea-ice leads in satellite data as a function of atmospheric conditions and measurement scale, *Ann. Glaciol.*, *17*, 227–232, 1993.

Key, J., J. A. Maslanik, and E. Ellefsen, The effects of sensor field-of-view on the geometrical characteristics of sea ice leads and implications for large-area heat flux estimates, *Remote Sens. Environ.*, *48*, 347–357, 1994.

Laursen, K., Passive broadband and spectral radiometric measurements available on NCAR/NSF research aircraft, *NCAR Tech. Bull. 25*, 1998.

Lindsay, R. W., Ice deformation near SHEBA, *J. Geophys. Res*, *107*, 10.1029/2000JC000445, in press, 2002.

Lindsay, R. W., and D. A. Rothrock, Arctic sea ice albedo from AVHRR, *J. Climate*, 1737–1749, 1994.

Lindsay, R. W., and D. A. Rothrock, Arctic sea ice leads from AVHRR images, *J. Geophys. Res.*, *100*, 4533–4544, 1995.

Marko, J. R., and R. E. Thomson, Spatially periodic lead patterns in the Canada Basin sea ice: A possible relationship to planetary waves, *Geophys. Res. Lett.*, *2*, 431–434, 1975.

Marko, J. R., and R. E. Thomson, Rectilinear leads and internal motions of the ice pack of the western Arctic Ocean, *J. Geophys. Res.*, *82*, 979–987, 1977.

Maslanik, J. A., and J. Key, On treatments of fetch and stability sensitivity in large-area estimates of sensible heat flux over sea ice, *J. Geophys. Res.*, *100*, 4573–4584, 1995.

Maslanik, J. A., C. Fowler, J. Key, T. Scambos, T. Hutchinson, and W. Emery, AVHRR-based Polar Pathfinder products for modeling applications, *Ann. Glaciol.*, *25*, 388–392, 1998.

Maslanik, J. A., J. Key, C. Fowler, and T. Nguyen, AVHRR-derived regional cloud and surface conditions during SHEBA and FIRE-ACE, *J. Geophys. Res.*, *106*, 15,233–15,249, 2001.

Maykut, G. A., Large-scale heat exchange and ice production in the central Arctic, *J. Geophys. Res.*, *87*, 7971–7984, 1982.

McLaren, A. S., The under-ice thickness distribution of the Arctic Basin as recorded by USS Nautilus in 1958 and USS Queenfish in 1970, *J. Geophys. Res.*, *94*, 4971–4983, 1989.

Miles, M. W., and R. G. Barry, A 5-year satellite climatology of winter sea ice leads in the western Arctic, *J. Geophys. Res.*, *103*, 21,723–21,734, 1998.

National Snow and Ice Data Center, *SHEBA Reconnaissance Imagery Version 1.0*, ARCSS Data Coord. Cent., Univ. of Colorado, Boulder, Colo., 2000.

Overland, J. E., B. A. Walter, and K. L. Davidson, Sea ice deformation in the Beaufort Sea, in *3rd Conf. on Polar Meteorol. and Oceanogr.*, Portland, Oregon, Am. Meteorol. Soc., Boston, Mass., 64–67, 1992.

Pegau, W. S., and C. A. Paulson, The albedo of Arctic leads in summer, *Ann. Glaciol.*, *33*, 221–224, 2001.

Perovich, D. K., et al., Year on ice gives climate insights, *EOS Trans.*, *80*, 481–486, 1999a.

Perovich, D. K., T. C. Grenfell, B. Light, J. A. Richter-Menge, M. Sturm, W. B. Tucker III, H. Eicken, G. A. Maykut, and B. Elder, *SHEBA: Snow and ice studies CD-ROM*, 1999b.

Scambos, T., T. Haran, C. Fowler, J. Maslanik, J. Key, and W. Emery, *AVHRR Polar Pathfinder Twice-Daily 1.25 km EASE-Grid Composites*, National Snow and Ice Data Center, Boulder, Colo., 2001.

Schramm, J. L., M. M. Holland, and J. A. Curry, Modeling the thermodynamics of a sea ice thickness distribution, 1. Sensitivity to ice thickness resolution, *J. Geophys. Res.*, *102*, 23,079–23,091, 1997.

Steffen, K., Fractures in arctic winter pack ice (north water, northern Baffin Bay), *Ann. Glaciol.*, *9*, 229–237, 1987.

Steffen, K., J. Key, D. J. Cavalieri, J. Comiso, P. Gloersen, K. St. Germain, and I. Rubenstein, The estimation of geophysical parameters using passive microwave algorithms, in *Microwave Remote Sensing of Sea Ice*, edited by F. D. Carsey, 1992.

Stroeve, J. C., J. E. Box, C. Fowler, T. Haran, and J. Key, Intercomparison between in situ and AVHRR Polar Pathfinder-derived surface albedo over Greenland, *Remote Sens. Environ.*, in press, 2001.

Wadhams, P., A. S. McLaren, and R. Weintraub, Ice thickness in Davis Strait in February from submarine sonar profiles, *J. Geophys. Res.*, *90*, 1069–1077, 1985.

Walter, B. A., and J. E. Overland, The response of lead patterns in the Beaufort Sea to storm-scale wind forcing, *Ann. Glaciol.*, *17*, 219–226, 1993.

J. A. Curry, School of Earth and Atmospheric Sciences, Georgia Institute of Technology, 221 Bobby Dodd Way, Atlanta, GA 30332-0340, USA.

M. A. Tschudi, NCAR — Research Aviation Facility, PO Box 3000, Boulder, CO 80307-3000, USA. (tschudi@ucar.edu)

J. A. Maslanik, Department of Aerospace Engineering Sciences, University of Colorado, Campus Box 429, Boulder, CO 80309 USA.